

ARTICLE

Open Access

A hierarchically ordered compacted coil scaffold for tissue regeneration

Yingchun Su^{1,2,3}, Zhongyang Zhang², Yilin Wan⁴, Yifan Zhang⁴, Zegao Wang^{3,5}, Lasse Hyldgaard Klausen^{3,6}, Peng Huang⁴, Mingdong Dong³, Xiaojun Han¹, Bianxiao Cui⁶ and Menglin Chen^{2,3}

Abstract

Hierarchically ordered scaffold has a great impact on cell patterning and tissue engineering. The introduction of controllable coils into a scaffold offers an additional unique structural feature compared to conventional linear patterned scaffolds and can greatly increase interior complexity and versatility. In this work, 3D coil compacted scaffolds with hierarchically ordered patterns and tunable coil densities created using speed-programmed melt electrospinning writing (sMEW) successfully led to in vitro cell growth in patterns with tunable cell density. Subcutaneous implantation in mice showed great in vivo biocompatibility, as evidenced by no significant increase in tumor necrosis factor α (TNF- α) and interleukin 6 (IL-6) levels in mouse serum. In addition, a lumbar vertebra was successfully printed for mesenchymal stem cells to grow in the desired pattern. A long-range patterned matrix composed of programmable short-range compacted coils enabled the design of complex structures, e.g., for tailored implants, by readily depositing short-range coil-compacted secondary architectures along with customized primary design.

Introduction

Cell therapy, especially stem-cell transplantation, has attracted extensive attention as a promising treatment for many diseases since the day it was proposed^{1–6}. In the typical process of cell transplantation, donor tissue is dissociated into individual cells, and then a proper scaffold is needed to support cell growth, differentiation or functionalization in vitro. Ultimately, the functional cells carried by the scaffold are implanted at the disease site to promote tissue repair or regeneration^{7,8}. To date, many three-dimensional (3D) porous scaffolds have been reported as structural supports for cells to promote attachment, proliferation, and differentiation, to yield functionally viable tissues as the ultimate goal^{9–11}. For example, incorporation of hydroxyapatite, a 3D porous composite scaffold, promoted osteogenic differentiation

and provided a favorable microenvironment for good neovascularization and tissue integration¹². Cell-laden peptide-tethered hydrogel scaffolds with a 3D porous architecture were applied for in vivo spinal cord recovery, which significantly facilitated nerve tissue integration and neuronal regeneration¹³. 3D porous scaffolds with interconnected pore networks provide efficient nutrient transport for cells with great potential in tissue engineering.

Electrospinning has recently become a widespread method to fabricate various fibrous scaffolds because of its easy operation and extracellular matrix mimicry^{14,15}. However, traditional solution electrospinning using organic solvent solutions usually forms random, dense, 2D fibrous mats unless a high-speed rotating collector or assisted electrical/magnetic field is used, and interspacing between adjacent fibers is uncontrollable^{16–19}. With lower conductivity, melt electrospinning generates a more stable jet than solution electrospinning, where solvent evaporation further introduces unstable factors. Recently, inspired by the three-dimensional (3D) printing technique, a melt electrospinning writing (MEW) process was proposed^{20–22}, by which

Correspondence: Mingdong Dong (dong@inano.au.dk) or Xiaojun Han (hanxiaojun@hit.edu.cn) or Menglin Chen (menglin@eng.au.dk)
¹State Key Laboratory of Urban Water Resource and Environment, School of Chemistry and Chemical Engineering, Harbin Institute of Technology, Harbin 150001, China
²Department of Engineering, Aarhus University, DK-8000 Aarhus C, Denmark
Full list of author information is available at the end of the article

© The Author(s) 2020

 **Open Access** This article is licensed under a Creative Commons Attribution 4.0 International License, which permits use, sharing, adaptation, distribution and reproduction in any medium or format, as long as you give appropriate credit to the original author(s) and the source, provide a link to the Creative Commons license, and indicate if changes were made. The images or other third party material in this article are included in the article's Creative Commons license, unless indicated otherwise in a credit line to the material. If material is not included in the article's Creative Commons license and your intended use is not permitted by statutory regulation or exceeds the permitted use, you will need to obtain permission directly from the copyright holder. To view a copy of this license, visit <http://creativecommons.org/licenses/by/4.0/>.

accurate positioning of submicron fibers that are ~2 orders of magnitude smaller than 3D printing has been realized. Depending on the collecting speed, these submicron fibers can be either collected as coils at low speed or be stretched into straight lines at high speed²³.

Poly-ε-caprolactone (PCL) has become the most popular scaffold material due to its nontoxicity, low melting point, good mechanical properties, and high biocompatibility^{24,25}. Many PCL-based scaffolds have been developed via MEW for tissue engineering applications^{26–37}: organized microfiber networks contribute to reinforcing hydrogels for chondrocyte differentiation³⁰; scaffolds with box-structured pores are adapted for the simultaneous seeding of multicellular spheroids^{31,32}; stretchable hexagonal microstructures can enhance the beating rate and cardiac maturation-related marker expression as a potential heart patch³³; and multiple layers of fibroblasts can be assembled with the aid of MEW scaffolds as a human prostate cancer microtissue model³⁴. Many researchers in tissue engineering have paid continuous attention to PCL scaffolds made by MEW.

Here, we present a hierarchically ordered PCL microfibrous architecture via speed-programmed melt electrospinning writing (sMEW). The periodicity and density of the coiling microfibers were tailored by virtue of coiling instability from electrohydrodynamics to achieve a secondary tunable structure along with the primary pattern design. Among many geometrical designs, rhombic geometry has been reported with interesting cellular responses^{38,39}. A variety of rhombic patterns were created after optimization of the stepped speed control over coil compactness during the printing process. The programmable speed control provides conventional MEW with an additional tailored secondary coiled structure, introducing tunable scaffold porosity and mechanical properties. Different from the conventional 3D porous scaffolds, which are produced by gas foaming, salt leaching or freeze-drying where the interconnected pore networks are dependent on the structure of porogen or phase separation, the porosity of the coil compacted 3D hierarchical architectures can be directly tailored by the stage speed and the layout of the design. The robustness of this technique to form lumbar vertebrae cellular microarrays with tunable density was investigated *in vitro*. The *in vivo* biocompatibility was investigated by surgical implantation into female athymic BALB/c nude mice.

Materials and methods

Preparation of PCL scaffolds

PCL pellets (Sigma-Aldrich, USA, Mn ~45 kDa) were loaded into a Spraybase melt electrospinning instrument (CAT000111, Ireland) and heated to 90 °C for 1 h to obtain a homogeneous polymer melt. The tip-collector distance, applied voltage, and pressure were 4 mm, 3.5 kV,

and 0.25 bar, respectively. The stage was supplied with high voltage, and a 30 G stationary, flat needle was grounded. Aluminum foil was placed on a flat-plate collector mounted on a programmable stage whose motion was controlled by UCCNC software (using G-code). The morphology of the cell-free PCL fibers was characterized by scanning electron microscopy (SEM, HITACHI, Japan, tabletop microscope) at an accelerating voltage of 15 kV. The critical translation speed (CTS) is the transition point between coiled and straight fibers, and after this point, the fibers are stretched by the movement of the collector⁴⁰. The design of a lumbar spine-like scaffold was fabricated by imitating the natural lumbar spine structure. The running G-code with running speeds of 200 mm/min for coils and 5000 mm/min for straight lines are shown in Supplementary note 6.

AFM colloid probe preparation

First, an OLYMPUS microcantilever (Olympus, Japan) was fixed in a micromanipulator. Through microcontrol by moving in the *x*, *y*, and *z* directions, the tip was slightly dipped in UV glue (Norland Optical Adhesives 65, USA) and immediately removed. Then, the dip-removal operation was repeated five times to obtain enough glue on the surface of the tip. After being covered with glue, the tip was moved to touch a single polystyrene particle (50 μm) until the polystyrene particle attached to the tip. Polystyrene particles were monodispersed on the cover glass with absolute ethanol (0.5 mL, VWR, USA) in advance. Finally, the cantilever was removed from the micromanipulator, and the cantilever was irradiated under a UV lamp (365 nm, VILBER-LOURMAT GmbH, Eberhardzell, Germany) to cure for 20 min. Each polystyrene particle-modified cantilever was examined by SEM before use.

Mechanical property measurements

The local mechanical properties of the specific rhombic-patterned scaffold were measured by AFM-based micro indentation under ambient conditions using a Nanoscope Multimode VIII system (Bruker, Santa Barbara, CA, USA). The cantilever sensitivity was calibrated by indenting the mica substrate. The force constant value *k* of the OLYMPUS microcantilever was experimentally determined before the mechanical experiments. The Derjaguin-Müller-Toporov (DMT) mechanical contact model was used for estimation of the local Young's modulus by Equation 1 from the withdrawal curves.

$$F = \frac{4}{3}E\sqrt{Rd^3} + F_{adh} \quad (1)$$

where *F* is the force acting on the cantilever, *F*_{adh} is the adhesion force between the probe and the scaffolds, *R* is the tip radius, *d* is the deformation of the scaffold, and *E* is Young's modulus.

Cell seeding and scaffold construct culture

Before cell seeding, PCL scaffolds (0.6 cm × 0.6 cm) were placed on the bottom of 96-well plates and sterilized with a UV lamp (252 nm, VILBER-LOURMAT GmbH, Eberhardzell, Germany) for 30 min. EGFP-hMSC-TERT cells (an immortalized human telomerase reverse transcriptase-transduced MSC line with an enhanced green fluorescent protein gene) were seeded at a density of 2.5×10^5 cells/mL (20 μ L). After culturing for 40 min under humid conditions at 37 °C with 5% CO₂, 100 μ L of Dulbecco's modified Eagle's medium-high glucose (DMEM with 4.5 g/L D-glucose, L-glutamine and pyruvate) supplemented with 10% fetal bovine serum and 1% penicillin–streptomycin was added, and the cells were cultured under humid conditions at 37 °C with 5% CO₂. After one day of adhesion, the scaffolds were transferred to new 96-well plates to measure the data absorption signal using a CCK-8 kit. New plates were used to ensure that the absorption signal was from the cells attached to the scaffolds rather than the cells on the bottom of plates. Before measuring the cell proliferation value on days 1, 3, 5, and 7, all the seeding scaffolds with cells were transferred to new 96-well plates. For the lumbar spine-like scaffold, 200 μ L of cells at a density of 2.5×10^5 cells/mL were seeded, and after 40 min of culture, the scaffolds were transferred to a new 24-well plate. The cell-laden scaffolds were fixed in 4% formaldehyde in PBS at room temperature for 20 min and treated with 0.2% Triton (Sigma-Aldrich, USA) in PBS for 15 min. Then, the cell-laden scaffolds were stained with Hoechst 33258 (Life Technologies, USA) for nuclear visualization. Cells adhered to the fibers were visualized by a Zeiss LSM 700 laser confocal microscope (Carl Zeiss Micro-Imaging GmbH, Germany) and an EVOS FL auto cell imaging system (Life Technologies, Carlsbad, CA, USA). The cytotoxicity test was performed by a lactate dehydrogenase (LDH) assay according to the kit manufacturer's instructions (Roche Diagnostics, Mannheim, Germany), and cell viability was determined by a cell counting kit (CCK-8, Dojindo, Japan). Cytotoxic properties quantified by the LDH assay are a reliable colorimetric reaction measurement at 490 nm to determine the amount of LDH in the media released from damaged cells. LDH activity release analysis was performed from the collected cultured media after 24 h of cell culture. The LDH activity of the cells cultured on TCP without or with 1% Triton X-100 was used as a low toxicity control (0% cell death) and high toxicity control (100% cell death), respectively. The cytotoxicity of the scaffolds was calculated using Equation 2.

$$\text{cytotoxicity}(\%) = \frac{\text{experimental value} - \text{low toxicity control}}{\text{high toxicity control} - \text{low toxicity control}} \times 100\% \quad (2)$$

Surgical implantation

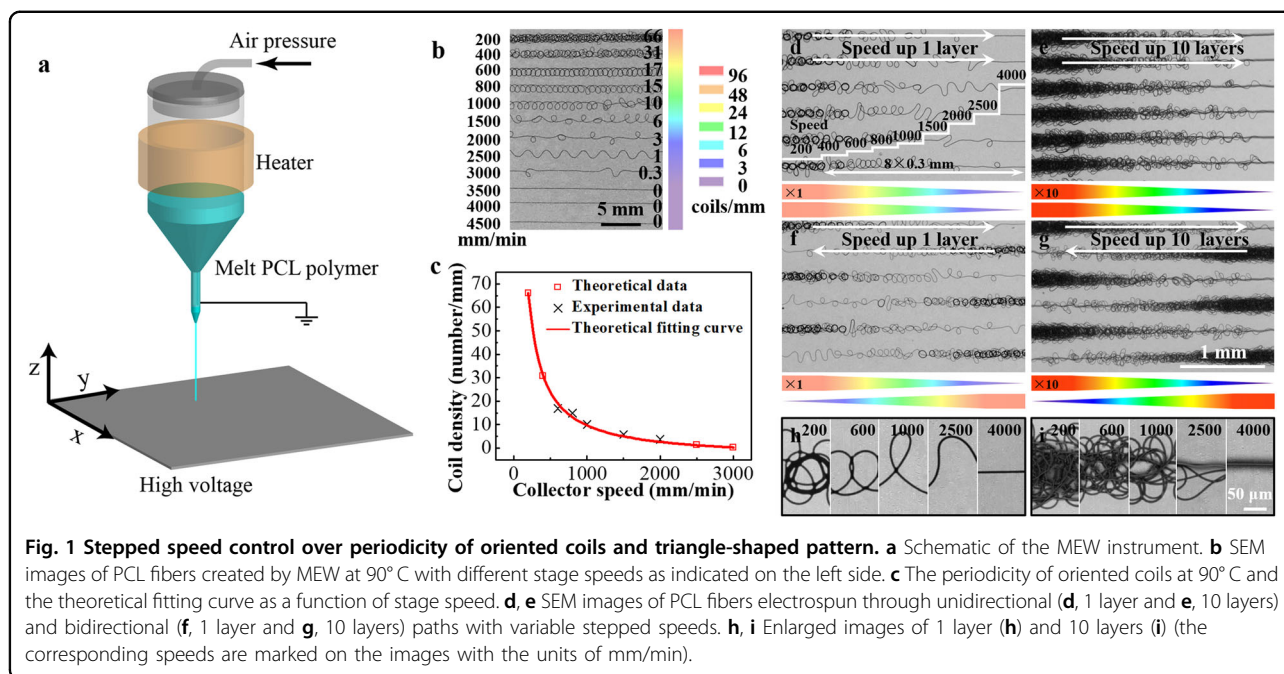
Female athymic BALB/c nude mice aged 4–6 weeks were purchased from Guangdong Medicinal Laboratory Animal Center (Guangzhou, China) and were used in accordance with the regulations of the Animal Ethical and Welfare Committee (AEWC) of Shenzhen University. Analysis was performed with three animals per group. A midline incision was made, and a subcutaneous pocket was created in the abdomen of each mouse in order to implant a 0.36 cm² (0.6 cm × 0.6 cm) piece of PCL scaffold. PCL sutures were used to close the incision, and then 0.5 mg/kg Baytril and 0.2 mg/kg Buprenex were administered for 3 days as an antibiotic and an analgesic, respectively. Serum samples were isolated from mouse blood before implantation and on days 3 and 7 after implantation and diluted for analysis. The concentrations of tumor necrosis factor α (TNF- α) and interleukin 6 (IL-6) in the supernatant were detected using the Mouse TNF- α and IL-6 ELISA kits (eBioscience, San Diego, USA) according to manufacturer-recommended procedures.

Results and discussion

Our MEW device, schematically represented in Fig. 1a, consisted of an air pressure pump, a heated extruder, a high voltage supply, and a moving stage collector. The morphologies of the PCL fibers extruded at 90 °C, under different stage speeds varying from 200 to 4500 mm/min were investigated (Fig. 1b). Inconsistent with the previously reported coiling instability from electrohydrodynamics^{32,35,41}, the fibers showed periodic coils at a low stage speed, lower coil density at an increased speed, and eventually turned into straight lines once the stage speed was increased above a threshold value, namely, the CTS^{23,42,43}. Hrynevich *et al.* provided details about the determination of the CTS value³². The CTS of the PCL fiber was approximately 3500 mm/min at 90 °C.

The periodic coil density was quantified and marked on the right side of the corresponding SEM images (Fig. 1b), assigned with a color bar. The coil density as a periodic property could be fitted as a function of the collector speed (Fig. 1c). For the coils printed at 90 °C, the fitting equations were proposed as Equation 3 and Equation 4 (the fitting computation process is shown in Supplementary note 1 and Fig. S1). From the equations, the theoretical numbers of coils at speeds of 200 mm/min and 400 mm/min (which cannot be manually counted due to experimental conditions) were 66 coils/mm and 31 coils/mm, respectively.

$$n = \frac{2sQ}{cV\pi r_1 r_2} - \frac{s}{c} \quad (3)$$



$$\text{Coil density} \frac{n}{s} = \frac{2Q}{cv\pi r_1 r_2} - \frac{1}{c} \quad (4)$$

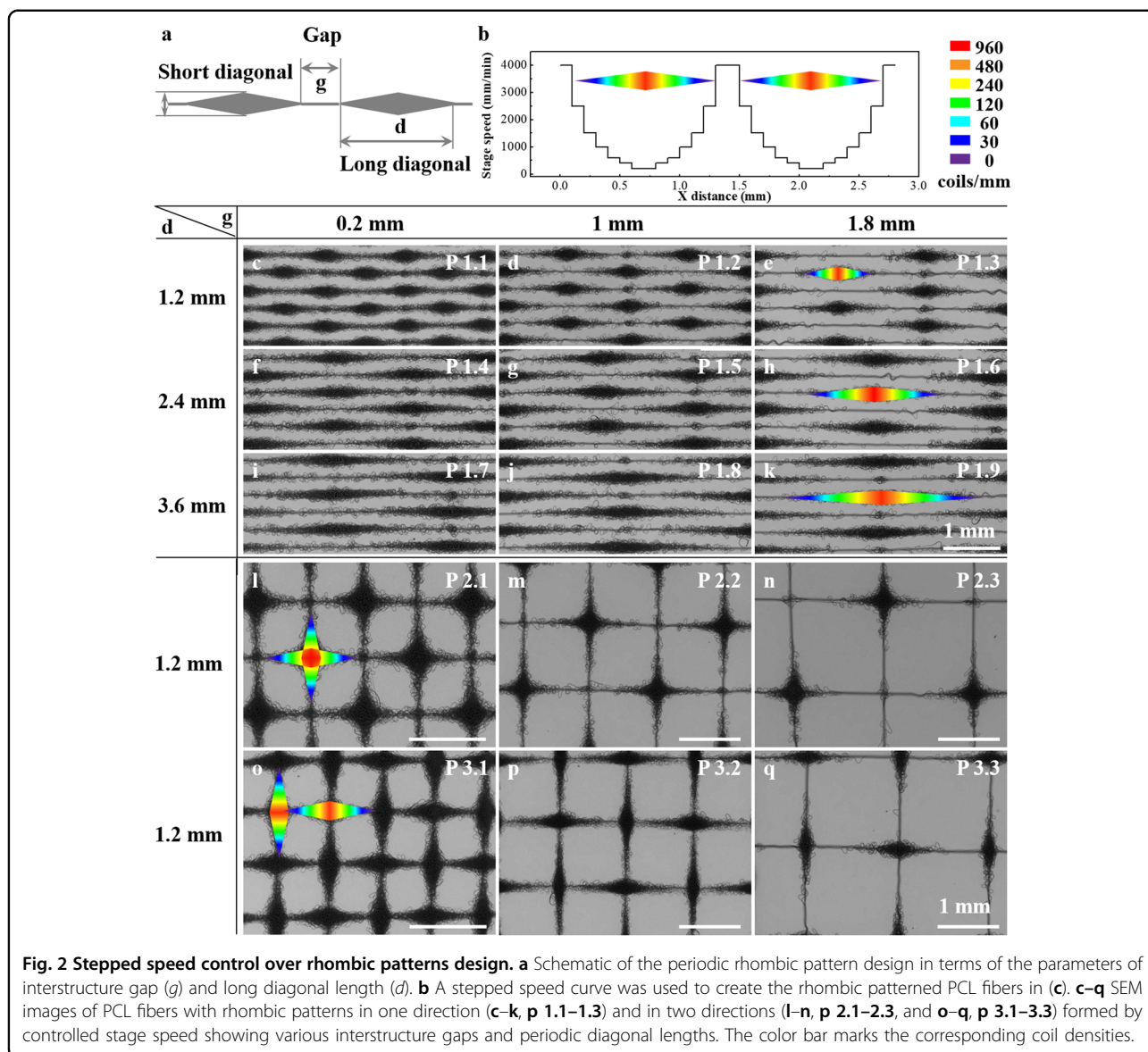
where s is the distance traveled by the collector; Q is the volume flow rate of the melted PCL; c is the course length of one coil; v is the collector speed; r_1 and r_2 are the minor and major axes of cross-section for fibers, respectively; n is the number of coils in distance “ s ”; and coil density (n/s) is the coil number per unit length.

Furthermore, the effects of temperature, distance, and applied voltage on the morphologies, diameters, and coil densities of the PCL fibers were also studied (Supplementary notes 2–3 and Figs. S2–3). With increased temperature, the PCL melt possessed lower viscosity and accordingly showed a higher flow rate, which led to an increase in the diameter. The effect of temperature, and collector speed on the diameter of straight PCL fibers was found to be consistent with previous studies^{44,45}. At the same stage speed (800, 1000 or 1500 mm/min), the PCL coil density increased linearly with temperatures from 75 °C to 100 °C (Fig. S2d). When the temperature was fixed at 90 °C and the distance/applied voltage increased from 4 mm, 3.5 kV to 16 mm, 6.5 kV, the coil density at 1000 mm/min increased from 10 coils/mm (Fig. 1c) to 37 coils/mm (Fig. S3f). The coil density along the stage orientation could also be tailored by both temperature and distance/applied voltage. It is noteworthy that Hochleitner et al. used a constant speed below the CTS to print sinusoidal patterns, where the wavelength and peak-to-peak distance of sinusoidal shapes were affected by the collector speed^{23,46}. The tubular structures of “figure of eight” looping and a sinusoidal fiber pattern were also

observed⁴⁷. Various designed soft networks with waving fibers were demonstrated for engineering biomechanically and biologically functional soft tissues⁴⁸. However, those studies applied constant speeds below the CTS, while various speeds (below the CTS) during printing have not been previously systematically explored.

Here, based on the established relationship between stage speed and coil density (Fig. 1b, c), a programmed stepped speed between 200 and 4000 mm/min was applied to print unidirectional (Fig. 1d, e) and bidirectional (Fig. 1f, g) parallel coil gradients. In Fig. 1d, the stage speed was increased from 200 to 4000 mm/min, and the distance between adjacent paths was 300 μm. The number of coils decreased with increasing stage speed and eventually disappeared. For the bidirectional path (Fig. 1f), the stage speed increased in one path from left to right and then inversely increased in the adjacent path. As shown in Fig. 1e, g, after repeating the unidirectional and bidirectional printing 10 times, macroscopic isosceles triangle-like patterns were created along each path. The enlarged images (Fig. 1h, i) showed the fiber morphologies at variable stepped speeds (200, 600, 1000, 2500, and 4000 mm/min) after printing 1 and 10 layers, respectively, where the single layer showed a similar result to that in Fig. 1b. Therefore, using programmed stage speed, triangle-shaped patterns with coil density gradients were successfully fabricated.

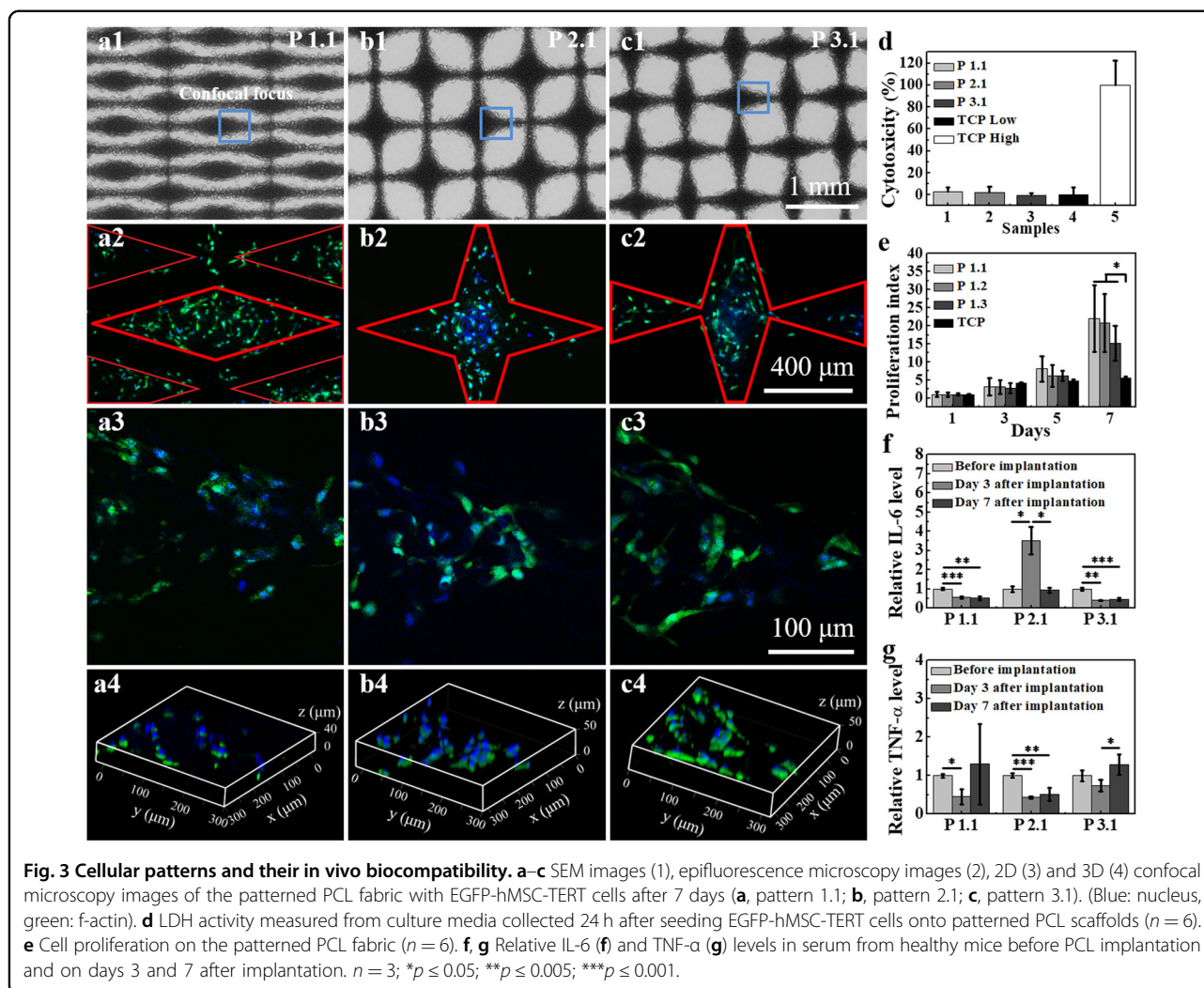
Next, by controlling the programmed stepped stage speed along the horizontal printing path, rhombic patterns with tunable geometry and coil density were successfully created. Different structures of the rhombic



patterns were characterized by each block having an interstructural gap (g) and a long periodic diagonal length (d) (Fig. 2a). To print the pattern with $g = 0.2$ mm and $d = 1.2$ mm, as an example, the stepped stage speed was programmed as shown in Fig. 2b. For each step distance of 0.1 mm, the speed gradually decreased from 4000 to 200 mm/min and then increased symmetrically back to 4000 mm/min to complete one rhombic structure. Various rhombic patterns (p 1.1–1.3) were produced through these blocks, as shown in Fig. 2e–k, with the corresponding stage speed program listed in Fig. S4. The length of the short diagonal for every rhombic structure was ~ 316 μm , which was determined by the intrinsic coiling instability, while g and d can be tailored by programming the stage speed. The faster the stage speed decreases/increases, the shorter d becomes. A total of 10 layers were

used for all patterns; accumulation of layers the corresponding to the pattern in Fig. 2e is shown from the SEM images in Fig. S5, which shows that not only the rhombic shape but also the 3D coil density can be controlled by the tunable layer number. Further combination of both horizontal and vertical printing with rhombus crossing at either their centers (p 2.1–2.3) or gaps (p 3.1–3.3) led to more sophisticated patterns with enhanced durability for practical handling. As shown in Fig. 2l–q, we created a structure with a constant periodic diagonal of 1.2 mm and a tunable inter structure gap from 0.2 to 1.8 mm. These scaffolds were complex systems composed of different patterns and coil compactness, which were arranged in the x and y directions with a highly ordered structure.

Furthermore, three rhombic structures ($g = 0.2$ mm, $d = 1.2$ mm) crossing with straight vertical lines, p 1.1,



vertical stepped speed printing crossing at the center, **p 2.1**, or at the gap, **p 3.1**, were used to assess cell patterning. SEM images of the three cell-free samples, epifluorescence imaging, and confocal fluorescence z-stack imaging for cell-laden samples are shown in Fig. 3a–c. sMEW technology provides a programmable speed-control strategy for the fabrication of fibrous patterned substrates with a proper 3D culture environment for cellular microarrays. The cells grown along the rhombic patterned scaffolds formed rhombic patterned cell constructs with a depth of $\sim 50 \mu\text{m}$.

Cytotoxicity tests (Fig. 3d) and cell proliferation experiments (Fig. 3e) were also conducted for these rhombic patterned scaffolds. All scaffolds showed toxicity lower than 6% with no significant differences compared to the tissue culture plastic (TCP) low control. It was observed that the initial cell proliferation from days 1 to 5 for cells cultured on the **p 1.1**, **2.1**, and **3.1** samples and TCP were similar, with no significant differences between

the groups. After 7 days of culture, cell proliferation in the **p 1.1**, **2.1**, and **3.1** groups was significantly accelerated compared to that of the TCP group, and showed excellent 3D cell culture capacity. No significance was found among the **p 1.1**, **2.1**, and **3.1** groups. The patterned scaffolds yielded high densities of viable cells, and the cell densities were sufficiently high to achieve multicellular architectures. The cell culturing process on grid scaffolds with speeds of 200 mm/min, 600 mm/min, 1000 mm/min, 2500 mm/min, and 4000 mm/min is also presented in Supplementary note 4 and Figs. S6–8. The day 1 adsorption values for all samples at 450 nm from the CCK-8 assay are given to show the initial cell attachment (Fig. S9). Last but not least, due to its flexibility, the scaffolds can also be used as injectable scaffolds (Video S1).

The **p 1.1**, **2.1**, and **3.1** scaffolds were evaluated in vivo by testing the IL-6 response in BALB/c mice for their special patterns. IL-6 is a pro-inflammatory cytokine with multiple functions and is believed to be a pivotal mediator

or host responder for injury and infection^{49,50}. TNF- α is another cytokine known to play an important role in cellular and inflammatory responses⁵¹. Overproduction of IL-6 causes neurological disease in the central nervous system⁵². Additionally, expression of TNF- α is related to nuclear factor- κ B that involved in tumour initiation and progression⁵³. Therefore, the inflammatory response from implantation of the patterned scaffolds was further evaluated by analyzing the relative expression (compared with each mouse group before implantation, considering the individual differences) of TNF- α and IL-6 in mouse serum from blood before implantation and on day 7 after implantation (Fig. 3f, g). For IL-6 expression, the **p 2.1** sample at day 7 showed no significant difference compared with the control group. IL-6 expression was significantly downregulated in groups **p 1.1** (from 17.03 to 8.88 pg/mL, a 0.52-fold change on day 7) and **p 3.1** (from 32.22 to 14.76 pg/mL, a 0.46-fold change on day 7). The expression levels of TNF- α from mouse serum in groups **p 1.1** and **p 3.1** before implantation and on day 7 showed no significant difference. For the **p 2.1** sample, the level of TNF- α secretion showed a significant reduction from 4.37 to 2.24 pg/mL (a 0.51-fold change). The expression levels, shown in Fig. S10, of TNF- α and IL-6 in mouse serum before implantation and on day 7 after implantation were

all in the normal range, confirming the biocompatibility of the PCL scaffolds^{54,55}.

The **p 2.1** samples exhibited significantly higher IL-6 expression than the **p 1.1** and **p 3.1** samples, possibly because the **p 2.1** scaffold is thicker (~120.8 μ m at the thickest point) than the **p 1.1** scaffold (~79.4 μ m at the thickest point) and **p 3.1** scaffold (~91.0 μ m at the thickest point). Previous reports have proposed that thicker materials could produce a proportionally higher magnitude of foreign body responses^{56,57}. The increasing expression of IL-6 from **p 2.1** on day 3 seemed to inhibit TNF- α protein expression, resulting in the downregulation of TNF- α levels on days 3 and 7. This is in agreement with the hypothesis proposed by Starkie et al.⁵⁸ that IL-6 can inhibit TNF- α protein production. In turn, the decrease in the IL-6 levels from the **p 1.1** and **p 3.1** samples also correlated with the upregulation of TNF- α expression with a lower inhibitory effect on day 7, where the level of TNF- α after implantation on the 7th day exhibited a slight increase compared with the control. On day 3, the TNF- α level exhibited the lowest expression as a transitional period.

In order to investigate the microscale mechanical properties of the hierarchical coil compacted scaffolds, a local compression test using atomic force microscopy (AFM) with a modified probe (Fig. 4a) was conducted.

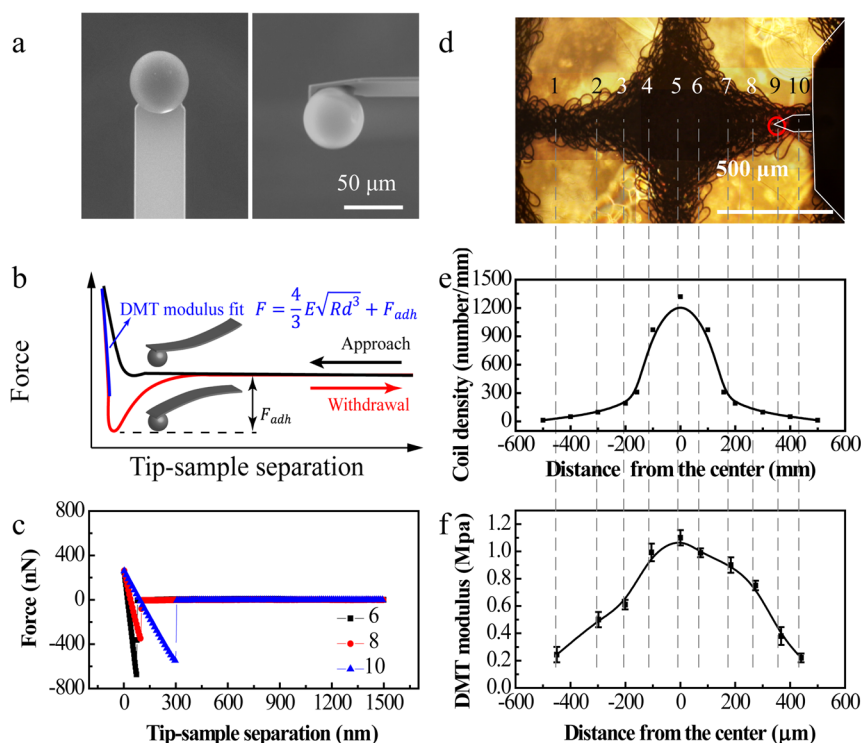
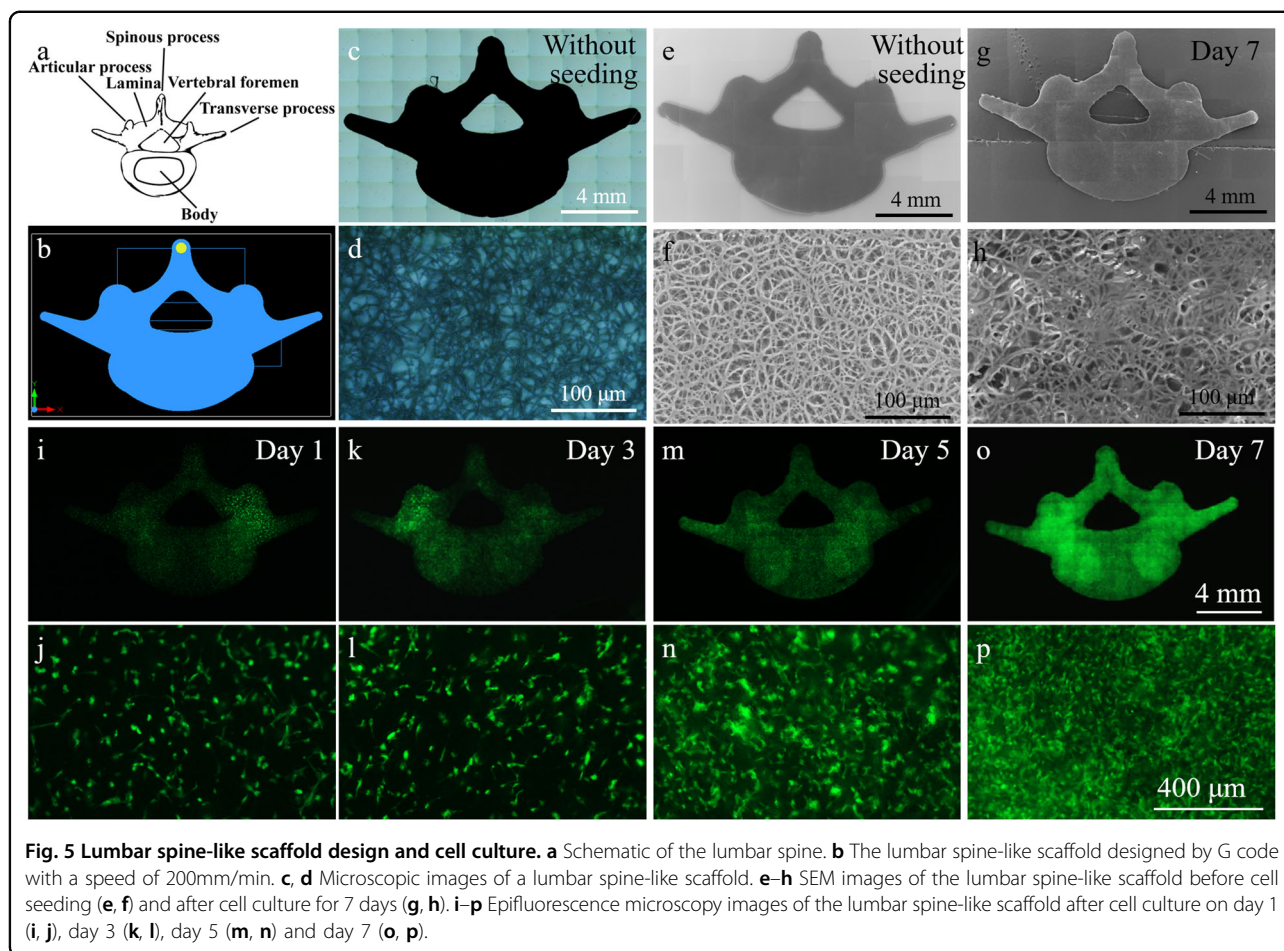


Fig. 4 Local mechanical property measurements for **p 2.1** scaffold. **a** SEM images of colloidal probes for local mechanical properties. **b** Schematic AFM-based force-distance curve (DMT model) and fitting equation. **c** AFM-based withdrawal force-distance curve at tip positions 6, 8, and 10. **d** Optical microscopy for the rhombic patterned sample to show the different tip positions. **e** Theoretical coil density for the rhombic patterned scaffold. **f** DMT modulus measured by AFM at different tip positions.



The mechanical properties were determined by micro-indentation using AFM. Young's modulus based on the Derjaguin–Muller–Toporov (DMT) model was calculated from the withdrawal curves using the equation in Fig. 4b, inset. Fig. 4d shows the tip locations on one rhombic pattern, where 10 points were measured. Representative withdrawal curves measured at marked positions 6, 8, and 10 are shown in Fig. 4c. With increasing coil density (Fig. 4e) from tip position 1 to tip position 5, the modulus of the scaffold (Fig. 4f) increased from 0.22 ± 0.03 MPa to 1.10 ± 0.06 MPa and then decreased back to 0.24 ± 0.06 MPa at tip position 10 with decreasing coil density (Fig. 4e). The Young's modulus data at each point were therefore presented (Fig. 4f) in correlation with the theoretical fiber density (Fig. 4e). The mechanical properties of the scaffolds were tunable based on the coil density. The tensile stress-strain curve measurements for the grid scaffolds with different speeds are also shown in Supplementary note 5 and Figs. S11–12. Such coil compacted scaffolds can be designed on top of customized primary shapes with tunable secondary interior structures and mechanical properties^{46,48}, which makes sMEW a great contribution to MEW technology.

To demonstrate the tailoring ability, a lumbar vertebra was printed using sMEW, according to the anatomical structure (Fig. 5a), with the design shown in Fig. 5b. The G code is shown in Supplementary note 6. The printed structure with a stage speed of 200 mm/min can be observed by optical microscopy (Fig. 5c) and SEM (Fig. 5e), where short-range compacted coils were also obtained (Fig. 5d, f). Because the running paths are too dense to observe the details in the 10- μ m design (Fig. 5b), the overall schematic diagram of G-code with 100 μ m spacing is shown in Fig. S13a, which can be helpful to observe the line and piece details clearly. The units of arcs and lines were used to fill in the simplified rectangular, parallelogram, round geometries with different sizes as small pieces. Then, these small pieces were assembled and connected with continuous printing to construct the whole vertebrae structure. The running path and corresponding zoomed-in SEM images of the lumbar spine-like scaffold (Fig. 5e) in different regions are shown in Fig. S13b–f, and all regions exhibited a similar coiling density. At the speed of 200 mm/min, the pore size was 9.13 ± 4.43 μ m, as shown in Fig. S7b, which is similar to the lacunar-canalicular pores surrounding the osteocytes that

are in the range of 0.1–10 μm ⁵⁹. After culturing with EGFP-hMSC-TERT cells for 7 days, the SEM images (Fig. 5g, h) revealed cell spreading on the scaffold (Fig. 5h). The lumbar spine-like scaffold-patterned EGFP-hMSC-TERT cells monitored by fluorescence microscopy on day 1 (Fig. 5i, j), day 3 (Fig. 5k, l), day 5 (Fig. 5m, n) and day 7 (Fig. 5o, p) showed cell proliferation over the culture time.

Conclusion

In summary, a hierarchically ordered 3D coil compacted scaffold was successfully prepared by using the sMEW method, in which variable long-range patterns and short-range tunable coil density can be readily achieved. Long-range macroscale shape mimicry is aimed at macroscale support for tissue engineering; moreover, with its abundant surface area and tunable mechanical properties, short-range tailored coil compactness can enhance microscale, cell-cell spatiotemporal modulation, and cell-extracellular matrix interactions. In addition to in vivo biocompatibility, hierarchically ordered scaffolds hold great potential for tissue engineering. Such a spatial arrangement of the cell containing coil structural building blocks could potentially facilitate the construction of complex tissues, such as lumbar vertebrae.

Furthermore, cells growing along the patterned biomaterials could generate a cellular microarray, which not only facilitates building tissues with similar or reinforced structural and functional characteristics^{60,61} but also offers the opportunity to model disease development and drug screening for precision medicine^{62–65}. Inspired by the cellular microarray reported for high-throughput toxicology assays⁶⁶ and anticancer drug screening⁶⁷ and assisted by metachip or a microfluidic chip, 3D coil compacted scaffolds with a cellular microarray might be used for early-stage drug discovery screening of drug candidates⁶⁸. It is also believed that spatially patterned scaffolds can provide unique systems to study cell behavior under complex microenvironments^{69–71}.

Supporting information

Supporting Information is available from the Online Library or from the author.

Acknowledgements

This work was supported by the Independent Research Fund Denmark, Aarhus University Research Foundation AUFF-E-2015-FLS-7-27, AUFF NOVA-project, Carlsberg Foundation, the EU H2020 RISE 2016 (MNR4SCell 734174), the National Natural Science Foundation of China (grant nos. 21929401 and 21773050), and the Natural Science Foundation of Heilongjiang Province for Distinguished Young Scholars (JC2018003). Y.S. thanks the Chinese Scholarship Council for financial support.

Author details

¹State Key Laboratory of Urban Water Resource and Environment, School of Chemistry and Chemical Engineering, Harbin Institute of Technology, Harbin 150001, China. ²Department of Engineering, Aarhus University, DK-8000 Aarhus C, Denmark. ³Interdisciplinary Nanoscience Center (iNANO), Sino-Danish

Center for Education and Research (SDC), Aarhus University, DK-8000 Aarhus C, Denmark. ⁴Guangdong Key Laboratory for Biomedical Measurements and Ultrasound Imaging, Laboratory of Evolutionary Theranostics, School of Biomedical Engineering, Health Science Center, Shenzhen University, Shenzhen 518060, China. ⁵College of Materials Science and Engineering, Sichuan University, Chengdu 610065, China. ⁶Department of Chemistry, Stanford University, Stanford, CA 94305, USA

Conflict of interest

The authors declare that they have no conflict of interest.

Publisher's note

Springer Nature remains neutral with regard to jurisdictional claims in published maps and institutional affiliations.

Supplementary information is available for this paper at <https://doi.org/10.1038/s41427-020-0234-7>.

Received: 23 January 2020 Revised: 21 March 2020 Accepted: 1 April 2020
Published online: 28 August 2020

References

- Suzuki, T. et al. Pulmonary macrophage transplantation therapy. *Nature* **514**, 450–454 (2014).
- Adil, M. M. et al. Dopaminergic neurons transplanted using cell-instructive biomaterials alleviate Parkinsonism in rodents. *Adv. Funct. Mater.* **28**, 1804144 (2018).
- June, C. H., Riddell, S. R. & Schumacher, T. N. Adoptive cellular therapy: a race to the finish line. *Sci. Transl. Med.* **7**, 280ps287 (2015).
- Forbes, S. J., Gupta, S. & Dhawan, A. Cell therapy for liver disease: from liver transplantation to cell factory. *J. Hepatol.* **62**, S157–S169 (2015).
- Hallett, P. J. et al. Successful function of autologous iPSC-derived dopamine neurons following transplantation in a non-human primate model of Parkinson's disease. *Cell Stem Cell* **16**, 269–274 (2015).
- Shin, J. et al. Mussel adhesion-inspired reverse transfection platform enhances osteogenic differentiation and bone formation of human adipose-derived stem cells. *Small* **12**, 6266–6278 (2016).
- Hirsch, T. et al. Regeneration of the entire human epidermis using transgenic stem cells. *Nature* **551**, 327–332 (2017).
- Gao, G. et al. Tissue engineered bio-blood-vessels constructed using a tissue-specific bioink and 3D coaxial cell printing technique: a novel therapy for ischemic disease. *Adv. Funct. Mater.* **27**, 1700798 (2017).
- Moroni, L. et al. Biofabrication strategies for 3D in vitro models and regenerative medicine. *Nat. Rev. Mater.* **3**, 21–37 (2018).
- Haugh, M. G. et al. Investigating the interplay between substrate stiffness and ligand chemistry in directing mesenchymal stem cell differentiation within 3D macro-porous substrates. *Biomaterials* **171**, 23–33 (2018).
- Nieto, A. et al. Three dimensional graphene foam/polymer hybrid as a high strength biocompatible scaffold. *Adv. Funct. Mater.* **25**, 3916–3924 (2015).
- Yang, Y. et al. Anti-infective efficacy, cytocompatibility and biocompatibility of a 3D-printed osteoconductive composite scaffold functionalized with quaternized chitosan. *Acta Biomater.* **46**, 112–128 (2016).
- Li, L. M. et al. Peptide-tethered hydrogel scaffold promotes recovery from spinal cord transection via synergism with mesenchymal stem cells. *ACS Appl. Mater. Inter.* **9**, 3330–3342 (2017).
- Slemming-Adamsen, P., Song, J., Dong, M., Besenbacher, F. & Chen, M. In Situ Cross-Linked PNPAM/Gelatin Nanofibers for Thermo-Responsive Drug Release. *Macromol. Mater. Eng.* **300**, 1226–1231 (2015).
- Wistlich, L. et al. Multimodal bioactivation of hydrophilic electrospun nanofibers enables simultaneous tuning of cell adhesivity and immunomodulatory effects. *Adv. Funct. Mater.* **27**, 1702903 (2017).
- Liu, Y. Q., Zhang, X. P., Xia, Y. N. & Yang, H. Magnetic-field-assisted electrospinning of aligned straight and wavy polymeric nanofibers. *Adv. Mater.* **22**, 2454–2457 (2010).
- Kongkhlang, T., Tashiro, K., Kotaki, M. & Chirachanchai, S. Electrospinning as a new technique to control the crystal morphology and molecular orientation of polyoxymethylene nanofibers. *J. Am. Chem. Soc.* **130**, 15460–15466 (2008).

18. Lee, M. Y. et al. Highly flexible organic nanofiber phototransistors fabricated on a textile composite for wearable photosensors. *Adv. Funct. Mater.* **26**, 1445–1453 (2016).
19. Kang, R. et al. Engineered three-dimensional nanofibrous multi-lamellar structure for annulus fibrosus repair. *J. Mater. Chem. B* **1**, 5462 (2013).
20. Brown, T. D., Dalton, P. D. & Hutmacher, D. W. Direct writing by way of melt electrospinning. *Adv. Mater.* **23**, 5651–5657 (2011).
21. Brown, T. D., Dalton, P. D. & Hutmacher, D. W. Melt electrospinning today: an opportune time for an emerging polymer process. *Prog. Polym. Sci.* **56**, 116–166 (2016).
22. Jørgensen, M. L. et al. A melt-electrowritten filter for capture and culture of circulating colon cancer cells. *Mater. Today Bio* **6**, 100052 (2020).
23. Hochleitner, G. et al. Fibre pulsing during melt electrospinning writing. *Bio-NanoMaterials* **17**, 159–171 (2016).
24. Taskin, M. B., Xia, D., Besenbacher, F., Dong, M. D. & Chen, M. L. Nanotopography featured polycaprolactone/polyethyleneoxide microfibers modulate endothelial cell response. *Nanoscale* **9**, 9218–9229 (2017).
25. Taskin, M. B. et al. Three-dimensional polydopamine functionalized coiled microfibrous scaffolds enhance human mesenchymal stem cells colonization and mild myofibroblastic differentiation. *ACS Appl. Mater. Inter.* **8**, 15864–15873 (2016).
26. Wunner, F. M. et al. Melt electrospinning writing of highly ordered large volume scaffold architectures. *Adv. Mater.* **30**, 1706570 (2018).
27. Farrugia, B. L. et al. Dermal fibroblast infiltration of poly(epsilon-caprolactone) scaffolds fabricated by melt electrospinning in a direct writing mode. *Biofabrication* **5**, 025001 (2013).
28. Bertlein, S. et al. Permanent hydrophilization and generic bioactivation of melt electrospun scaffolds. *Adv. Healthc. Mater.* **8**, 1801544 (2019).
29. Hochleitner, G. et al. Additive manufacturing of scaffolds with sub-micron filaments via melt electrospinning writing. *Biofabrication* **7**, 035002 (2015).
30. Visser, J. et al. Reinforcement of hydrogels using three-dimensionally printed microfibres. *Nat. Commun.* **6**, 6933 (2015).
31. McMaster, R. et al. Tailored melt electrospun scaffolds for the generation of sheet-like tissue constructs from multicellular spheroids. *Adv. Healthc. Mater.* **8**, 1801326 (2019).
32. Hrynevich, A. et al. Dimension-based design of melt electrospun scaffolds. *Small* **14**, 1800232 (2018).
33. Castilho, M. et al. Melt electrospinning allows tailored microstructural and mechanical design of scaffolds to advance functional human myocardial tissue formation. *Adv. Funct. Mater.* **28**, 1803151 (2018).
34. Pereira, B. A. et al. Tissue engineered human prostate microtissues reveal key role of mast cell-derived tryptase in potentiating cancer-associated fibroblast (CAF)-induced morphometric transition in vitro. *Biomaterials* **197**, 72–85 (2019).
35. Bertlein, S. et al. Development of endothelial cell networks in 3D tissues by combination of melt electrospinning writing with cell-accumulation technology. *Small* **14**, 1701521 (2018).
36. Muerza-Cascante, M. L. et al. Endosteal-like extracellular matrix expression on melt electrospun written scaffolds. *Acta Biomater.* **52**, 145–158 (2017).
37. Zhang, Y., Zhang, Z., Wang, Y., Su, Y. & Chen, M. 3D myotube guidance on hierarchically organized anisotropic and conductive fibers for skeletal muscle tissue engineering. *Mat. Sci. Eng. C-Mater.* **116**, 111070 (2020).
38. Rudrich, U. et al. Pre-osteoblast cell colonization of porous silicon substituted hydroxyapatite bioceramics: Influence of microporosity and macropore design. *Mat. Sci. Eng. C-Mater.* **97**, 510–528 (2019).
39. Eichhorn, M., Stannard, C., Anselme, K. & Ruhe, J. Nucleus deformation of SaOs-2 cells on rhombic mu-pillars. *J. Mater. Sci.-Mater. M* **26**, 108 (2015).
40. Hochleitner, G., Hummer, J. F., Luxenhofer, R. & Groll, J. High definition fibrous poly(2-ethyl-2-oxazoline) scaffolds through melt electrospinning writing. *Polymer* **55**, 5017–5023 (2014).
41. Castilho, M. et al. Melt electrospinning writing of poly-hydroxymethylglycolide-co-epsilon-caprolactone-based scaffolds for cardiac tissue engineering. *Adv. Healthc. Mater.* **6**, 1700311 (2017).
42. Brun, P. T., Audoly, B., Ribe, N. M., Eaves, T. S. & Lister, J. R. Liquid ropes: a geometrical model for thin viscous jet instabilities. *Phys. Rev. Lett.* **114**, 174501 (2015).
43. Welch, R. L., Szeto, B. & Morris, S. W. Frequency structure of the nonlinear instability of a dragged viscous thread. *Phys. Rev. E* **85**, 066209 (2012).
44. Wunner, F. M. et al. Printomics: the high-throughput analysis of printing parameters applied to melt electrospinning. *Biofabrication* **11**, 025004 (2019).
45. Haigh, J. N., Dargaville, T. R. & Dalton, P. D. Additive manufacturing with polypropylene microfibers. *Mat. Sci. Eng. C-Mater.* **77**, 883–887 (2017).
46. Hochleitner, G. et al. Melt electrospinning below the critical translation speed to fabricate crimped elastomer scaffolds with non-linear extension behaviour. Check for oPdetes mimicking that of ligaments and tendons. *Acta Biomater.* **72**, 110–120 (2018).
47. Jungst, T. et al. Melt electrospinning onto cylinders: effects of rotational velocity and collector diameter on morphology of tubular structures. *Polym. Int.* **64**, 1086–1095 (2015).
48. Bas, O. et al. An integrated design, material, and fabrication platform for engineering biomechanically and biologically functional soft tissues. *ACS Appl. Mater. Inter.* **9**, 29430–29437 (2017).
49. Wang, C. et al. Immunological responses triggered by photothermal therapy with carbon nanotubes in combination with anti-CTLA-4 therapy to inhibit cancer metastasis. *Adv. Mater.* **26**, 8154–8162 (2014).
50. Harker, J. A., Lewis, G. M., Mack, L. & Zuniga, E. I. Late interleukin-6 escalates T follicular helper cell responses and controls a chronic viral infection. *Science* **334**, 825–829 (2011).
51. Tostanoski, L. H. et al. Design of polyelectrolyte multilayers to promote immunological tolerance. *ACS Nano* **10**, 9334–9345 (2016).
52. Hunter, C. A. & Jones, S. A. IL-6 as a keystone cytokine in health and disease. *Nat. Immunol.* **16**, 448–457 (2015).
53. Mantovani, A., Allavena, P., Sica, A. & Balkwill, F. Cancer-related inflammation. *Nature* **454**, 436–444 (2008).
54. Kang, H. W. et al. A 3D bioprinting system to produce human-scale tissue constructs with structural integrity. *Nat. Biotechnol.* **34**, 312–322 (2016).
55. Nasajpour, A. et al. A multifunctional polymeric periodontal membrane with osteogenic and antibacterial characteristics. *Adv. Funct. Mater.* **28**, 1703437 (2018).
56. Veisoh, O. et al. Size- and shape-dependent foreign body immune response to materials implanted in rodents and non-human primates. *Nat. Mater.* **14**, 643–651 (2015).
57. Ward, W. K., Slobodzin, E. P., Tiekotter, K. L. & Wood, M. D. The effect of microgeometry, implant thickness and polyurethane chemistry on the foreign body response to subcutaneous implants. *Biomaterials* **23**, 4185–4192 (2002).
58. Starkie, R., Ostrowski, S. R., Jauffred, S., Febbraio, M. & Pedersen, B. K. Exercise and IL-6 infusion inhibit endotoxin-induced TNF-alpha production in humans. *Faseb. J.* **17**, 884–886 (2003).
59. Tonar, Z., Khadang, I., Fiala, P., Nedorost, L. & Kochova, P. Quantification of compact bone microporosities in the basal and alveolar portions of the human mandible using osteocyte lacunar density and area fraction of vascular canals. *Ann. Anat.* **193**, 211–219 (2011).
60. Huh, D. et al. Reconstituting organ-level lung functions on a chip. *Science* **328**, 1662–1668 (2010).
61. Wang, S. F. et al. Molecularly engineered biodegradable polymer networks with a wide range of stiffness for bone and peripheral nerve regeneration. *Adv. Funct. Mater.* **25**, 2715–2724 (2015).
62. Pati, F., Gantelius, J. & Svahn, H. A. 3D bioprinting of tissue/organ models. *Angew. Chem. Int. Ed.* **55**, 4650–4665 (2016).
63. Joung, D. et al. 3D printed stem-cell derived neural progenitors generate spinal cord scaffolds. *Adv. Funct. Mater.* **28**, 1801850 (2018).
64. Berthuy, O. I., Blum, L. J. & Marquette, C. A. Cells on chip for multiplex screening. *Biosens. Bioelectron.* **76**, 29–37 (2016).
65. Meli, L., Jordan, E. T., Clark, D. S., Linhardt, R. J. & Dordick, J. S. Influence of a three-dimensional, microarray environment on human Cell culture in drug screening systems. *Biomaterials* **33**, 9087–9096 (2012).
66. Lee, M. Y. et al. Three-dimensional cellular microarray for high-throughput toxicology assays. *Proc. Natl Acad. Sci. USA* **105**, 59–63 (2008).
67. Hsiung, L. C. et al. Dielectrophoresis-based cellular microarray chip for anticancer drug screening in perfusion microenvironments. *Lab Chip* **11**, 2333–2342 (2011).
68. Jimenez-Moreno, N., Stathakos, P., Caldwell, M. A. & Lane, J. D. Induced pluripotent stem cell neuronal models for the study of autophagy pathways in human neurodegenerative disease. *Cells* **6**, 24 (2017).
69. Aguilar, J. P. et al. 3D Electrophoresis-assisted lithography (3DEAL): 3D molecular printing to create functional patterns and anisotropic hydrogels. *Adv. Funct. Mater.* **28**, 1703014 (2018).
70. Jin, X. F. & Riedel-Kruse, I. H. Biofilm lithography enables high-resolution cell patterning via optogenetic adhesion expression. *Proc. Natl Acad. Sci. USA* **115**, 3698–3703 (2018).
71. Kim, W., Kim, M. & Kim, G. H. 3D-printed biomimetic scaffold simulating microfibril muscle structure. *Adv. Funct. Mater.* **28**, 1800405 (2018).